variable appearing in a given function and defined over a continuous domain, rather than on a few points only.

The existence of allotropic modifications would seem to complicate analyses of this sort. Temperature hysteresis makes most physical properties multiple-valued functions, and hence the history of the specimen must be specified. Even then, there is some question as to whether the transition temperature T_c follows the law $T_c\bar{M}^{\frac{1}{2}}=$const. In our experiments the precision in the region of the martensitic transition in lithium ($\sim$80°K) was not high enough to pick up definite manifestations of the transition.[17] Certain irregularities in our data below 80°K might be attributable to a modification of the crystal structure. But all of our data were taken with temperature increasing from 4.2°K, and it is likely that hysteresis would have produced anomalies at temperature considerably above the transition temperature 80°K. We can state only that the effect of the martensitic transition is not discernible in our measurements.

IV. SUMMARY

a. Isotopic Mass

By studying the temperature dependence of the intrinsic resistance, normalized with respect to room-temperature resistance, of isotopically pure specimens Li^6 and Li^7 in the range 4°–300°K, it was established that

(1) the Bloch-Grüneisen equation gives the qualitative features of the temperature dependence of resistance; and

(2) the resistivity ρ divided by a characteristic temperature Θ, a parameter inversely proportional to the square root of the isotopic mass M, is a universal function of T/Θ; or, which is the same thing, of $TM^{\frac{1}{2}}$.

b. Isotopic Composition

By studying the temperature dependence of the normalized intrinsic resistance of isotopic alloys made with varying proportions of Li^6 and Li^7 in the range 4°–300°K, it was established that

(1) the general course of the temperature dependence of the resistance of isotopic alloys can be described only semiquantitatively by the Bloch-Grüneisen equation; and

(2) the resistivity ρ divided by a characteristic temperature Θ, a parameter inversely proportional to the square root of the average isotopic mass $\bar{M}$, is a universal function of T/Θ (or of $T\bar{M}^{\frac{1}{2}}$). The data do not permit a preference to be established between arithmetic-mean mass and the harmonic-mean mass.

c. General Considerations

(1) The electrical resistivity of solid isotopic alloys of any composition, including the limiting case of pure isotopes, can be obtained from knowledge of the temperature dependence of the absolute resistivity of a single alloy, by means of a simple scaling factor, the square root of the ratio of the average masses, applied to the resistivity and to the temperature.

(2) Isotopic impurities do not seem to act as additional scattering sources, but serve only to modify the lattice-vibrational spectra.

(3) The existence of allotropic modifications should complicate the behavior of electrical resistance in lithium, but such an effect was not discernible in our experiments.

[17] See, e.g., D. L. Martin, Physica **25**, 1193 (1959).

PHYSICAL REVIEW VOLUME 126, NUMBER 1 APRIL 1, 1962

Range of Heavy Ions in Solids*

D. Powers and W. Whaling
California Institute of Technology, Pasadena, California
(Received November 20, 1961)

The ranges of N, Ne, Ar, Kr, and Xe ions in Be, B, C, and Al have been measured to ±10% for incident ion energy 50–500 kev. A monoenergetic ion beam from an electrostatic accelerator strikes a thick target of the absorber, and the penetration depth is determined by a momentum analysis of monoenergetic protons elastically scattered from the target and the embedded atoms. An expression relating the penetration depth to the actual path length is derived. A linear range-energy behavior is found for Ar, Kr, and Xe ions; for N and Ne ions dE/dX increases with ion energy. The experimental ranges are 20% shorter than theoretical values based on energy loss by elastic nuclear collisions. By including electronic contributions to the stopping process, good agreement with experiment is achieved.

I. INTRODUCTION

BOHR laid the foundation for a theoretical description of the energy loss of heavy ions of low velocity in his 1948 paper,[1] and his analysis of the stopping process in terms of elastic nuclear collisions has since been extended by Nielsen[2] and by Lindhard and Scharff.[3] In spite of the increased use of accelerated heavy ions in recent years, there are very few experi-

* Supported in part by the Joint Program of the Office of Naval Research and the U. S. Atomic Energy Commission.

[1] N. Bohr, Kgl. Danske Videnskab. Selskab., Mat.-Fys. Medd **18**, No. 8 (1948).

[2] K. O. Nielsen, in *Electromagnetically Enriched Isotopes and Mass Spectrometry*, edited by M. L. Smith (Academic Press Inc., New York, 1956), p. 68.

[3] J. Lindhard and M. Scharff, Phys. Rev. **124**, 128 (1961).

mental measurements with which to test these theoretical treatments of the subject, and all but one of the existing measurements apply to gaseous absorbers. The present experiment was undertaken to fill this gap in the experimental information on the stopping process to test the applicability of the existing theory to the energy loss of heavy ions in solid absorbers.

II. EXPERIMENTAL METHOD

Singly charged heavy ions were produced in the conventional radio-frequency ion source of our 600-kev electrostatic accelerator. The accelerator is equipped with an electrostatic beam energy analyzer which holds the beam constant and monoenergetic within $\pm 0.2\%$. Before entering the electrostatic analyzer the beam was deflected magnetically to select the desired mass and charge component. The resolution of the magnetic deflector was not sufficient to separate individual isotopes of the Ne, Ar, Kr, and Xe, and we assume that the beam had the normal isotopic composition. The electrostatic analyzer was calibrated against the $F^{19}(p,\alpha\gamma)O^{16}$ resonance at 340.5 ± 0.3 kev.

The ion beam was examined on a quartz plate and defocused to provide an approximately uniform coverage of a target spot of 0.5 cm^2. The average ion beam current over the target spot did not exceed 9 μa/cm^2; fluctuations in the intensity and distribution of the beam current may have produced occasional current densities ten times greater. The total charge deposited varied from 530 to 46 000 μcoulomb/cm^2 of singly charged ions.

After the target had been bombarded with heavy ions, the gas entering the ion source was changed to hydrogen and within a few minutes a proton beam was available. The proton beam was trimmed to strike a small (0.01 cm^2) part of the target area irradiated with heavy ions. The targets were normally not removed from the target chamber between heavy ion bombardment and the proton scattering which followed immediately. On one occasion a 48-hr delay following argon bombardment of beryllium indicated no detectable diffusion of the argon in the elapsed interval.

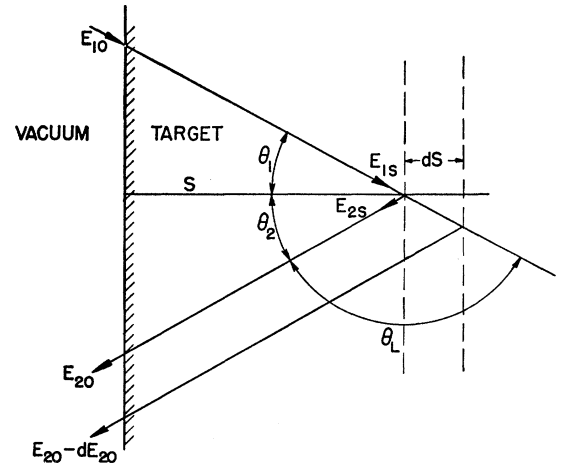

FIG. 1. The proton scattering geometry. E_{10} is the proton beam energy, E_{1S} and E_{2S} are the proton energies immediately before and after scattering, E_{20} is the energy at which protons are detected in the spectrometer.

Protons elastically scattered from the target at a laboratory angle of 129° were analyzed in momentum with an 8-in. double-focusing magnetic spectrometer. The 0.031-in. collecting slit of the spectrometer provided a momentum resolution $P/\Delta P$ of approximately 800. The spectrometer was calibrated against the electrostatic analyzer energy scale by observing the protons elastically scattered at a known angle from targets of known composition. The charge incident upon the target during the ion bombardment or the proton scattering was measured with a current integrator.

The target chamber contained two liquid nitrogen traps, one immediately surrounding the target with small apertures for incident and scattered particles, the other between the diffusion pump and the target chamber, to minimize the deposition of pump vapor on the target surface. The pressure in the target chamber was $\sim 10^{-6}$ mm Hg.

Thick targets of commercial grade Be and Al were polished with graded abrasives down to 4/0 emery polishing paper, then finished with red rouge polishing compound on a soft cloth moistened with kerosene. The targets were washed several times in alcohol and distilled water and examined under a microscope to see that no visible surface scratches were present. The carbon targets, $\frac{1}{16}$-in.-thick disks machined from a graphite spectroscope electrode, were polished with 4/0 emery polishing paper, but a microscopically smooth surface could not be obtained on the soft graphite targets. The boron targets were made by cracking diborane (B_2H_6) on highly polished tungsten targets heated inductively to 600°C in an atmosphere of the gas. Normal isotopic boron was used in some targets; other boron targets contained 96% B^{10}. Analysis of target composition, described in Sec. III, revealed 1% of oxygen in the Be targets, 3% oxygen in the C targets, and 2% Fe, Cu, or Mn in some of the Al targets.

III. ANALYSIS OF EXPERIMENTAL DATA

Analysis of surface composition by proton scattering has been described in detail by Rubin[4] and by Brown *et al.*[5] Their method has been adapted in the present experiment to determine the depth beneath the target surface of a known impurity. Figure 1 illustrates the geometry of the proton scattering. A monoenergetic proton beam of energy E_{10} enters the target at angle θ_1 with respect to the surface normal and penetrates to a perpendicular distance S beneath the surface. The protons are then elastically scattered through an angle

[4] S. Rubin, Nuclear Instr. and Methods **5**, 177 (1959).
[5] A. B. Brown, C. W. Snyder, W. A. Fowler, and C. C. Lauritsen, Phys. Rev. **82**, 159 (1951).

θ_L and emerge from the target with energy E_{20} and at an angle θ_2 with respect to the surface normal. The proton energy at the distance S beneath the surface can be written as:

$$E_{1S}=E_{10}-\int_{X=S/\cos\theta_1}^{X=0}(dE/dX)dX, \quad (1)$$

where (dE/dX) is the rate of proton energy loss along the path X. We denote by M_1 and M_0 the proton mass and target atom mass, respectively. If E_{1S} and E_{2S} are the proton energies immediately before and after the scattering event, then $E_{2S}=\alpha E_{1S}$, where

$$\alpha^{\frac{1}{2}}=\frac{M_1\cos\theta_L}{M_1+M_0}+\left[\left(\frac{M_1\cos\theta_L}{M_1+M_0}\right)^2+\frac{M_0-M_1}{M_0+M_1}\right]^{\frac{1}{2}}. \quad (2)$$

The energy E_{2S} at the distance S beneath the surface is related to the energy E_{20} with which the protons emerge from the target by

$$E_{2S}=E_{20}+\int_{X=0}^{X=S/\cos\theta_2}(dE/dX)dX. \quad (3)$$

Combining (1) and (3) by means of the relation $E_{2S}=\alpha E_{1S}$, one obtains

$$E_{20}=\alpha E_{10}-\alpha\int_{S/\cos\theta_1}^{0}(dE/dX)dX-\int_{0}^{S/\cos\theta_2}(dE/dX)dX, \quad (4)$$

which relates E_{10}, E_{20}, S, M_0, and M_1.

In the procedure followed in this experiment, E_{20} is fixed by the magnetic spectrometer. All the angles are fixed, and E_{10} is varied to discover those particular values for which protons are detected in the spectrometer. Each such value of E_{10} determines by Eqs. (2) and (4) a relation between the mass of the scattering nucleus M_0 and the depth S at which the scattering occurs. Neither M_0 nor S is determined explicitly without further information, but in practice the target composition and expected contaminants are known, and furthermore, thin layers of contamination are almost always surface layers with $S=0$. Atoms distributed in the target over a range of S are indicated by scattered protons at a continuum of E_{10} values. A typical experimental result of the scattering of protons from a clean Be target (i.e., before heavy ion bombardment) is indicated by the dashed curve in Fig. 2, where the number of protons detected in the spectrometer per incident proton is plotted as a function of E_{10}. Such curves are referred to as momentum profiles for the target. Scattered protons which are detected at $E_{10}=324$, 353, and 379 kev can be identified with $S=0$ and $M_0=28$, 16, and 12, respectively. These peaks arise from surface contamination of the target. The continuum beginning at $E_{10}=415$ kev marks a distribution of nuclei with mass nine beginning at $S=0$ and extending into the Be target.

The solid curve in Fig. 2 shows the momentum profile after the target had been bombarded with 39 000 μcoul/cm^2 of N^+ ions. It is reasonable to identify the broad peak centered around $E_{10}=507$ kev with mass $M_0=14$, and Eq. (4) then determines the distance S at which these ions are embedded in the beryllium. The breadth of the distribution indicates that the nitrogen is distributed over a region of S values as a result of range straggling. The buildup of C and Si layers on the surface during the bombardment is seen through the enlargement of these peaks in the profile. The displacement of the Be^9 step is due to the increased proton energy required to penetrate the surface layers of Si and C deposited during the bombardment. The shift in the O^{16} peak indicates a thin layer of oxygen on the surface of the Be.

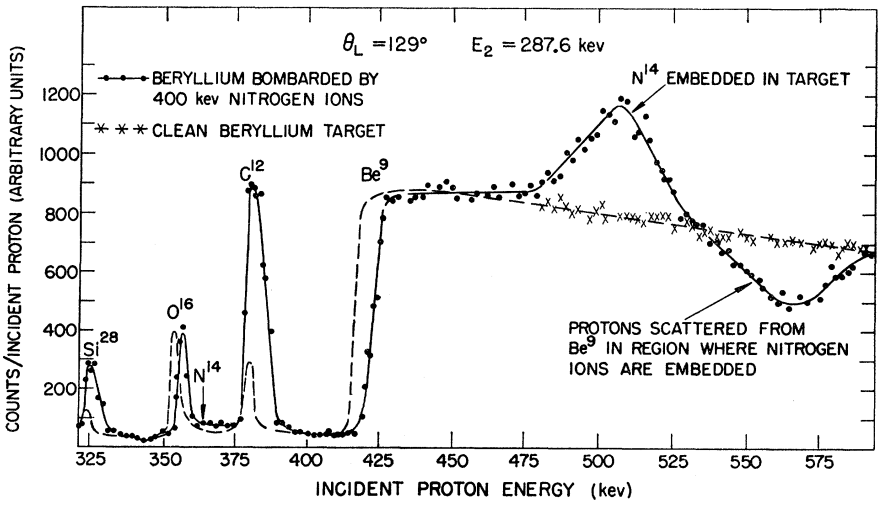

FIG. 2. The number of protons scattered at a laboratory angle of 129° with energy 287.6 kev as a function of incident proton energy. The dashed curve was measured before, the solid curve after, the Be target had been bombarded with 39 000 microcoulombs/cm^2 of 400-kev N^+ ions. The experimental points have been omitted from the dashed curve where they would interfere with the solid curve. The symbols designate the incident proton energy at which protons scattered from Si^{28}, O^{16}, N^{14}, C^{12}, and Be^9 on the target surface would be detected in the spectrometer.

The integrals in Eq. (4) can be evaluated numerically if the composition of the target is known as a function of the depth S, since the proton stopping cross sections are known or can be estimated with good accuracy.[6] If the concentration of embedded atoms is negligible, as in our measurements with Ar, Kr, and Xe ions, the integrals may be approximated (to within 1% in this experiment) by evaluating the integrand at the intermediate energies $E^1=(E_{10}+E_{1S})/2$ and $E^2=(E_{2S}+E_{20})/2$. Equation (4) may then be rearranged to give the expression with which we convert our experimental observations into range values when embedded atom concentration is negligible:

$$t\equiv\rho S=(\alpha E_{10}-E_{20})M_0 \times\cos\theta_1[\alpha\epsilon(E^1)+(\cos\theta_1/\cos\theta_2)\epsilon(E^2)]^{-1},$$

where $\epsilon=-(dE/NdX)$ is the atomic stopping cross section for protons in the target material, N is the number of target atoms per unit volume, and ρ is the density of the target material.

An alternative method of locating the embedded atoms makes use of protons scattered from the target material. The yield of scattered protons detected in the spectrometer is that from a thin lamina of the target of thickness $dS/\cos\theta_1$, where dS is related to dE_{20}, the spectrometer energy window, by $dS=dE_{20}/(dE_{20}/dS)$. The complete expression for dE_{20}/dS, given in Appendix A, is rather cumbersome, but it is clearly dependent upon dE/dX at a depth S in the target. The embedded atoms increase dE/dX and hence reduce the yield observed with the spectrometer, as may be seen in Fig. 2 at $E_{10}=565$ kev. The penetration depth S can be obtained from this dip in precisely the same manner as from the peak. When the straggling is large or the mass difference between target and embedded atom is small, the peak and dip may overlap to some extent. Such interference was observed in this experiment with N in C, N in Al, and Ne in C. The separate contribution of protons scattered from target atoms and from embedded atoms can be determined with the aid of the thick target yield formulas of Appendix A.

IV. EFFECT OF EMBEDDED ATOMS ON RANGE

After prolonged bombardment the concentration of foreign atoms embedded in the target may reach significant values, and it is necessary to consider whether atoms deposited at the beginning of the ion bombardment affect the range of ions which subsequently penetrate the target. Four different spots on a Be target were bombarded with 300-kev Kr ions in amounts ranging from 60 to 900 μcoul/cm^2. From target profiles taken at these four spots, $N_{\mathrm{Kr}}/N_{\mathrm{Be}}$, the concentration by number of Kr atoms at the peak of the distribution, was determined by means of the thick target yield equation (A4). Concentrations $N_{\mathrm{Kr}}/N_{\mathrm{Be}}<0.03$ did not affect the location of the peak in the profile within our experimental accuracy, whereas the concentrations actually used in Kr range determinations varied from 0.001 to 0.003. Xe, Kr, and Ar atoms were detectable in the target at maximum concentrations $N_I/N_T=0.03$ or less, and at these low concentrations we have neglected their contribution to dE/dX for protons in Eq. (4), and we assume that the presence of the embedded atoms does not alter the range of the heavy ions subsequently hitting the target.

Concentrations as large as 0.60 were required in some of our measurements with N and Ne ions, and our procedure for computing ranges was altered to make allowance for the embedded atoms. The target was divided into two regions: (1) the region extending from the surface down to the measurable depth at which the embedded atom distribution began, corresponding to energy $E_{10}=475$ kev in Fig. 2; and (2) the region over which the embedded atoms are distributed. Region 1 is composed of pure target, and its depth can be evaluated from Eq. (4). Region 2 contains a distribution of embedded atoms increasing from zero at the boundary of the region to a maximum concentration $(N_I/N_T)_{\max}$ at the peak. We have approximated this distribution in region 2 with a uniform distribution of embedded atoms with a concentration of $0.5(N_I/N_T)_{\max}$. The range in region 2 is computed from Eq. (4) with E_{10} and E_{20} replaced by the energy of protons as they enter and leave region 2, and (dE/dX) includes a contribution from the embedded atoms in region 2. The width of region 1 is a range in pure target material, but the distance from the boundary of region 2 to the peak of the distribution gives a range in a mixture of target and embedded atom which can be converted to range in pure target by $R_T=R_{\mathrm{mix}}[1+(N_I/N_T)(\epsilon_I/\epsilon_T)]$, and the resultant range in pure target is added to the range in region 1 to obtain the total range. For the ratio ϵ_I/ϵ_T in the expression above, we have used the value computed from Nielsen's expression, Eq. (8). This analysis which takes into account the embedded atoms yields a range smaller than that obtained by neglecting the embedded atoms by at most 2% for our neon measurements and 8% for our nitrogen measurements.

V. SURFACE LAYER CORRECTIONS TO PROTON AND ION ENERGIES

The deposition of contamination on the surface of the target during the ion and proton bombardment can affect our measurements in two ways. First, the incident ions lose energy in the contamination layer and strike the target with energy less than the bombarding energy. Second, the protons lose energy in going through this layer twice, and E_{10} and E_{20} must be corrected to take account of this loss of energy. The layer thickness increases during the course of the measurements, and the thickness and composition of the layer at any time, as well as the stopping cross sections for protons and heavy

[6] W. Whaling, *Handbuch der Physik*, edited by S. Flügge (Springer-Verlag, Berlin, 1958), Vol. 34, p. 193.

ions in the contaminating materials, must be known in order to allow for the effect of this surface layer.

The energy loss of protons in the contamination layer is determined from the displacement of the target step in the momentum profile after bombardment with a known charge density of ions and protons. Figure 2 shows the displacement of the Be step before and after ion bombardment. The observed displacement represents the sum of ΔE_{10} and ΔE_{20}, plus a small change in the recoil energy imparted to the scattering nucleus. Both ΔE_{10} and ΔE_{20} can be determined individually from the known energy dependence of the proton stopping cross section in the contaminating material. For example in Fig. 2, which happens to be the largest displacement observed in our experiment, $\Delta E_{10}=2.6$ kev, and $\Delta E_{20}=3.8$ kev.

The composition of the contaminating material is determined by the standard methods of surface composition analysis by proton scattering.[4] As may be seen in Fig. 2, the contamination consists of C and Si from the diffusion pump. We assume that the proton scattering cross section for C and Si is given by the Rutherford formula at these proton energies so that the area under the contaminant peaks is proportional to $N_x Z_x^2/E_x^2$, where N_x is the number of atoms in the layer with atomic number Z_x and E_x is the bombarding energy at which scattering from contaminant x is observed. The relative area under the contaminant peaks determines the ratio $N_{\mathrm{Si}}/N_{\mathrm{C}}$.

The energy loss ${}_I\Delta E$ of the heavy ion in passing through a layer in which the proton loses energy ${}_p\Delta E$ is given by

$$ {}_I\Delta E/{}_p\Delta E=[{}_I\epsilon_{\mathrm{C}}+(N_{\mathrm{Si}}/N_{\mathrm{C}})\,{}_I\epsilon_{\mathrm{Si}}]/[{}_p\epsilon_{\mathrm{C}}+(N_{\mathrm{Si}}/N_{\mathrm{C}})\,{}_p\epsilon_{\mathrm{Si}}], $$

where ϵ is the stopping cross section per atom, the left subscript p and I refer to proton and heavy ion, and the right subscript refers to the stopping material. The proton stopping cross sections are known or can be estimated to within a few percent.[6] The heavy-ion stopping cross sections in carbon were obtained by differentiating our experimental range-energy relation for N, Ne, and Ar ions in carbon, and extrapolating this experimental value by means of the theoretical mass and charge dependence of Eq. (8) to obtain the heavy-ion stopping cross section in Si and for other incident ions.

Since the initial layer thickness is zero, the average value ${}_I\Delta E$ is taken to be one-half of the final value. In Fig. 2 the average energy loss of the 400-kev ions in the layer was 16.1 kev. The ion energy correction is subject to some uncertainty since it depends on stopping cross sections that have not been measured and varies with time. It is gratifying that the magnitude of this correction was usually less than 2% of the ion energy. The correction is largest at the low bombarding energy; for 50-kev ions the correction exceeded 5% for the following measurements: 6% for N in Al, 8% for Kr in Be, 10% for Ne in Be and Ar in B^{10}, and 34% for Xe in Be.

VI. RANGE STRAGGLING

We define the range straggling parameter Ω to be the full width at half maximum of the distribution of embedded atoms in the target. The difference δE_{10} between the bombarding energy at the half-height points on the embedded atom peak in the momentum profile is a measure of this distribution, but δE_{10} also includes contributions from the finite instrumental resolution δ_{inst}, and from the proton energy straggling δ_p. If we define δ by the relation $\delta^2=\delta E_{10}^2-\delta_{\mathrm{inst}}^2-\delta_p^2$, then $\Omega=\rho(dR/dE_{10})\delta$.

The instrumental resolution δ_{inst}, the width at half maximum of the proton peak observed with the spectrometer when protons are scattered from an infinitely thin target, arises from the finite beam spot size and collector slit width, from inhomogeneity in incident beam energy, and from the variation of scattered proton energy with angle over the $\Delta\theta_L$ aperture of the spectrometer. This last mentioned contribution to δ_{inst} depends on the mass of the scattering atom, and it is convenient to write

$$ \delta_{\mathrm{inst}}^2=\tfrac{2}{3}(\ln 2)[\alpha^{-1}(dE_{20}/d\theta_L)\Delta\theta_L]^2+\delta_0^2. $$

The term δ_0, which includes all contributions to δ_{inst} other than the $\Delta\theta_L$ term, is constant, and by writing δ_{inst} in this way one can allow for the variation of δ_{inst} with mass of the scattering atom. The dependence of α on M_0 is given by Eq. (2). The width ΔE_{10} of the target step in the momentum profile provides an experimental value of δ_{inst} for a particular M_0 by the relation $\delta_{\mathrm{inst}}^2=(4\ln 2)(\Delta E_{10})^2/\pi$, and δ_{inst} may be computed for any other M_0.

The proton energy straggling contribution δ_p was obtained from Bohr's expression[1] for the mean-square deviation $\sigma_B^2=4\pi e^4 N Z_0 R$ in the energy of an initially monoenergetic proton beam after passing through an absorber of thickness R containing N atoms/cm^3 of atomic number Z_0. Measurements[7] of the energy straggling of protons in our energy range are consistent with Bohr's expression. The incident proton straggling over the path $R=S/\cos\theta_1$ is reduced by a factor $\alpha=dE_2/dE_1$ in the scattering event and added to the straggling over the emergent path $S/\cos\theta_2$ to find the total deviation in E_{20} given by

$$ \sigma_B^2(E_{20})=\alpha^2\sigma_B^2(S/\cos\theta_1)+\sigma_B^2(S/\cos\theta_2). $$

Expressed in terms of E_{10} we obtain, after converting σ into the full width at half maximum:

$$ \delta_p^2=2(4\ln 2)4\pi e^4 N Z_0 S \times\left[\frac{{}_p\epsilon(E_{10})}{{}_p\epsilon(E_{20})}\frac{{}_p\epsilon(E_{2S})}{{}_p\epsilon(E_{1S})}\frac{1}{\alpha}\right]^2\left[\frac{\alpha^2}{\cos\theta_1}+\frac{1}{\cos\theta_2}\right]. $$

[7] C. B. Madsen and P. Venkateswarlu, Phys. Rev. **74**, 1782 (1948).

TABLE I. Experimental uncertainty in the measurement of N ranges in Be.

	Source of error	Probable error (%)	Probable error in range from this source (%)
E_{10}	Location of peak in profile	±0.5–0.6	±8–2
E_{20}	Drift of spectrometer setting	0.21	2–0.4
E_{10}	Electrostatic analyzer drift	0.2	2–0.3
E_{10}, E_{20}	Electrostatic analyzer calibration	0.2	0.3
E_{10}, E_{20}	Uncertainty in surface contamination correction	20	3–1
$\cos\theta_1$	Uncertainty in θ_1	0.9	0.3
$\cos\theta_2$	Uncertainty in θ_2	0.9	0.6
ϵ	Uncertainty in proton stopping cross section	3	3
α	Uncertainty in θ_L	0.2	3–0.6
E_{10}	Uncertainty in proton energy as it enters region 2	0.2–0.8	0.1
$(N_I/N_T)_{\max}$	Uncertainty in scattering cross section; use of $0.5(N_I/N_T)_{\max}$ as average impurity concentration in region 2	50	2–1
$I\epsilon_I/I\epsilon_T$	Theoretical extrapolation of measured values	20	0.3–0.2
Root-mean-square probable error: ±10–4%			

Very low energy ions stop so near the surface that S for the lower half maximum may differ significantly from the value at the upper half-maximum point. In such cases, we evaluate δ_p at both points and compute the correction to each half of the observed distribution separately.

In our measurements the magnitude of δ_p and δ_{inst} were such that δ, from which the straggling was finally computed, differed from the observed δE_{10} by as much as 40%, although the difference was generally less than 6%. It should be noted that by our definition Ω represents the distribution in *projected* ranges along the direction of the initial velocity of the ion; it does not represent the distribution of the actual path lengths. Lindhard and Scharff[3] state that these two distributions should not differ greatly when $M_1 \gg M_0$.

VII. ACCURACY

The sources of experimental error are listed in Table I. The parameters entering in the calculation of the range appear in the first column followed by the source of uncertainty in the value of the parameter. The middle column lists the probable error in percent for each parameter, and the last column shows how this uncertainty contributes to the probable error of the range. The particular values listed are those for N ions in Be, but they are typical of all other measurements except that the last three sources of error are absent from measurements with Ar, Kr, and Xe ions, since the embedded atom concentration was negligible. When two numbers appear in the second and third columns, the first refers to 50-kev N ions, the last to 500-kev ions; values at intermediate energies generally decrease with increasing ion energy. The total probable error is the sum of the squares of the individual errors. Although several of the parameters are poorly known, they contribute small uncertainties to the final range. For all measurements, the principal uncertainty is in the location of the peak of the broad distribution of protons scattered from the embedded atoms.

The uncertainty in the ion energy arises principally from the energy loss in the contamination layer. Our assumption that the average layer thickness is one-half its final value has been assigned an uncertainty of 50%, and other sources of error increase the total uncertainty in the ion energy loss in the layer to about 60%. Fortunately, the surface contamination is so small that the resultant uncertainty in ion energy is usually less than 1%.

VIII. RESULTS

The ranges and range straggling measured in this experiment are presented in Table II. The heavy ions Ar, Kr, and Xe show the constant rate of energy loss expected from Nielsen's discussion of energy loss by elastic nuclear collisions. For the N and Ne ions, which are moving with greater velocity, dE/dR increases with ion energy. The relatively small straggling of the N ions in C and Al is inconsistent with a nuclear collision stopping process which leads to large straggling when $M_1 \lesssim M_0$ because of large-angle scattering. Both the small straggling and the increasing dE/dR can be understood qualitatively if electronic excitation and ionization contribute to the stopping of the N and Ne ions.

The range measured in this experiment is the projection along the initial beam axis of the actual path length that the ion follows in the target. Theoretical discussions of the stopping process lead to expressions for the actual path length, and we must take this difference into account in comparing our results with the theory. The difference between the path length R and the projected path length R_p may be expressed[8]:

$$R-R_p=\frac{1}{2}\int_0^R \langle\Theta^2(l)\rangle_{\text{av}}dl, \tag{5}$$

where $\langle\Theta^2(l)\rangle_{\text{av}}$, the mean-square deviation in angle from the initial beam axis at a distance l along the path, is given by[9]

$$\langle\Theta^2(l)\rangle_{\text{av}}=\int_0^l dl\int_0^\infty N\theta_L^2(p)2\pi p dp. \tag{6}$$

$\theta_L(p)$ is the laboratory scattering angle for interactions

[8] H. Bichsel, R. F. Mozley, and W. A. Aron, Phys. Rev. **105**, 1788 (1957).

[9] E. Fermi, *Nuclear Physics*, notes compiled by J. Orear, A. H. Rosenfeld, and R. A. Schluter (University of Chicago Press, Chicago, Illinois, 1950), p. 52.

TABLE II. Experimental values of the range and range straggling. The uncertainties listed are probable errors. When no uncertainty is listed, the probable error is less than 1%.

Ion and target	Ion energy (kev)	Range (μg/cm^2)	Range straggling (μg/cm^2)
Xe in Be	32.4±9.4	4.3± 1.2	4.4± 1.1
	100.3	9.4± 1.0	6.0± 1.1
	200.5	17.3± 1.2	10.1± 1.3
	300.8	24.0± 1.8	12.1± 1.7
	401.0	32.0± 2.0	21.3± 1.8
	501.3	41.1± 5.1	19.3± 1.9
Xe in Al	50.1	4.3± 0.9	4.4± 1.5
	100.3	7.7± 1.4	11.3± 1.5
	200.5	15.2± 2.0	17.7± 2.0
	300.8	22.8± 2.8	30.9± 3.3
	401.0	36.6± 3.3	33.7± 3.2
	501.3	43.7± 4.9	30.3± 6.0
Kr in Be	45.9±3.0	5.8± 1.0	3.9± 1.3
	96.0±3.2	10.6± 1.5	8.7± 1.1
	196.2±3.6	23.4± 2.3	16.6± 2.0
	295.6±4.2	35.5± 3.7	21.1± 3.4
	395.6±5.0	48.2± 4.4	28.4± 4.6
	495.6±5.8	60.7± 4.0	26.4± 6.2
Kr in Al	50.1	5.0± 1.4	6.9± 2.1
	100.3	9.1± 2.2	15.3± 1.8
	200.5	19.2± 1.7	19.0± 3.1
	300.8	35.2± 4.0	28.5± 3.9
	401.0	47.4± 6.4	38.9± 6.5
	501.3	56.1± 7.6	45.2± 8.9
Ar in Be	48.5±1.0	8.7± 2.2	8.2± 1.2
	98.6±1.4	18.5± 2.0	14.2± 1.7
	198.8±2.1	36.0± 3.3	21.0± 2.5
	298.0±3.3	56.7± 4.0	25.7± 3.7
	396.9±4.3	72.8± 5.0	30.9± 4.5
	500.2	97.3± 6.5	37.8± 5.0
Ar in B^{10}	44.7±3.0	8.2± 2	...
	99.6±1.1	15.9± 2.0	12.4± 2.4
	300.2	50.0± 3.9	22.9± 2.7
	500.2	82.4± 7.3	26.7± 8.7
Ar in B	49.6±0.6	9.2± 2	...
	100.2	19.0± 1.7	11.4± 1.4
	249.5	44.6± 2.8	17.2± 2.5
	300.0	55.6± 3.9	26.1± 3.3
	500.3	86.6± 5.8	22.9± 8.0
Ar in C	49.9	10.4± 2.7	7.5± 1.5
	100.0	18.1± 2.6	13.4± 1.5
	201.0	36.7± 4.1	19.6± 2.2
	300.0	49.2± 4.0	20.0± 4.4
	400.0	64.6± 7.4	28.9± 8.1
	500.0	86.0± 5.9	27.2± 5.6
Ne in Be	45.2±2.7	14.1± 2.9	12.3± 2.1
	95.7±2.5	41.7± 3.4	19.8± 3.0
	194.6±3.5	72.7± 6.5	33.9± 3.9
	296.6±3.6	108.9± 4.2	...
	393.7±5.5	134.1±10.7	41.9± 9.9
	490.5±7.4	155.1± 9.9	42.0± 6.7
Ne in C	50.1	17.9± 2.1	17.4± 2.9
	99.6±1.1	38.3± 2.7	15.4± 4.7
	200.2	75.2± 4.1	24.2± 6.8
	299.7	100.4± 7.0	30.2±12.5
	400.5	127.3± 8.2	40.3±10.8
	500.6	143.7± 9.5	31.1±10.7
N in Be	48.3±1.3	23.8± 2.3	11.0± 1.8
	97.5±1.9	40.9± 2.6	12.5± 3.5
	195.5±3.6	76.5± 4.5	23.2± 5.6
	291.3±6.3	103.1± 5.8	23.1± 5.5
	385.9±9.6	127.6± 5.3	23.7± 6.2
	492.3±7.6	151.2± 6.1	17.0± 5.7
N in C	49.9	24.0± 3.6	14.3± 3.9
	99.7±1.1	43.4± 3.2	20.9± 6.0
	199.6	75.7± 6.7	31.5±11.4
	300.0	100.9± 5.8	30.1±12.2
N in Al	46.7±2.1	30.8±10.0	39.9±10.8
	100.1	74.0± 8.3	22.2±10.1
	200.2	114.1±12.8	44.1±12.5
	296.2±3.6	156.1±14.2	62.9±16.0
	400.5	198.7±15.1	42.8±14.6
	497.4±5.4	218.5±16.8	57.2±16.8

at impact parameter p, and N is the number density of target atoms. Nielsen[2] derives an expression for the scattering angle in the center-of-mass system for heavy-ion scattering, from which we obtain in the limit $M_1 \gg M_0$, $\theta_L = (M_0/M_1)\sin[\pi/(1+ba/2.718p^2)^{\frac{1}{2}}]$; b is the collision diameter, and the screening parameter used by Nielsen is $a=\hbar^2/[m_0e^2(Z_0^{\frac{2}{3}}+Z_1^{\frac{2}{3}})^{\frac{1}{2}}]$. With this expression for θ_L, Eq. (6) becomes

$$\langle\Theta^2(l)\rangle_{\rm av}=2.493N\left(\frac{\hbar^2}{m_0}\right)\frac{Z_0Z_1}{(Z_0^{\frac{2}{3}}+Z_1^{\frac{2}{3}})^{\frac{1}{2}}} \times\frac{M_0(M_0+M_1)}{M_1^2}\frac{1}{(dE/dl)}\ln\frac{E(0)}{E(l)}, \quad (7)$$

where $E(l)$ is the ion energy at a distance l along the path, and dE/dl for the ion is given by Nielsen's theory:

$$dE/dl=3.63\frac{NM_1}{(M_0+M_1)}\frac{Z_0Z_1}{(Z_0^{\frac{2}{3}}+Z_1^{\frac{2}{3}})^{\frac{1}{2}}}\frac{\hbar^2}{m_0}. \quad (8)$$

When Eq. (7) for $\langle\Theta^2(l)\rangle_{\rm av}$ is substituted in Eq. (5), the integration yields

$$R-R_p=\frac{1.247N}{dF/dl}\left(\frac{M_0}{M_1}\right)^2\frac{M_0+M_1}{M_0}\frac{Z_0Z_1}{(Z_0^{\frac{2}{3}}+Z_1^{\frac{2}{3}})^{\frac{1}{2}}}\frac{\hbar^2}{m_0}R, \quad (9)$$

which gives $R/R_p \approx 1+M_0/2.90M_1$ in the limit of $M_1/M_0 \gg 1$.

Lindhard and Scharff[3] have pointed out that $\mathfrak{R}=RNM_0 4\pi a^2M_1/(M_0+M_1)^2$ and $\mathcal{E}=a/b$ are useful parameters with which to express the range-energy

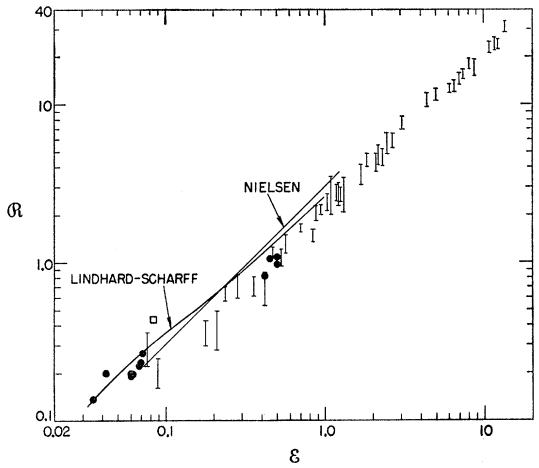

FIG. 3. Experimental values of $\mathfrak{R}=RNM_0 4\pi a^2 M_1(M_0+M_1)^{-2}$ as a function of $\varepsilon=aEM_0[Z_1Z_0e^2(M_0+M_1)]^{-1}$. The vertical lines indicate the probable error for the measurements with Ar, Kr, and Xe ions in this experiment. The circles are the measurements in gases by Valyocsik[10] and by Baulch and Duncan.[11] The square is Davies measurement[12] of the range of 50-kev Cs^{137} ions in Al. All ranges have been corrected with Eq. (9) to give ion path length. The straight line is the range-energy relation of Nielsen,[2] the curve is that of Lindhard and Scharff.[3]

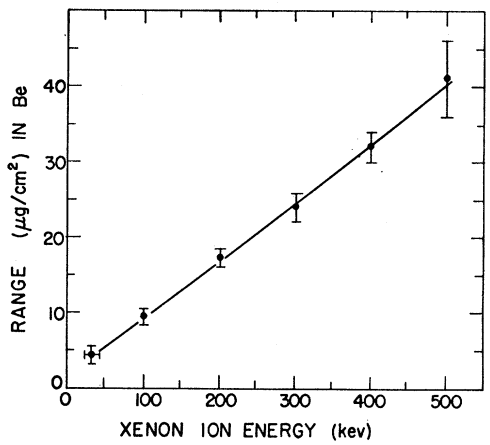

FIG. 4. The curve is the theoretical range-energy relation which includes both electronic and elastic nuclear collision contributions to the stopping. The experimental values have been corrected to give ion path length with Eq. (9).

relation when electronic contributions are not important. The value of the screening parameter used by Lindhard is $a=0.885(\hbar^2/m_0e^2)(Z_0^{\frac{2}{3}}+Z_1^{\frac{2}{3}})^{-\frac{1}{2}}$, and the collision diameter is $b=2Z_1Z_0e^2(M_0+M_1)/(M_0M_1v^2)$, where v is the laboratory velocity of the incident ion. Expressed in these parameters, Nielsen's range-energy expression becomes $\mathfrak{R}=3.06\mathcal{E}$, and he proposes that the approximations used in his derivation should be valid in the interval $0.068\leq\mathcal{E}\leq1.21$. The straight line in Fig. 3 is a plot of Nielsen's expression.

Lindhard and Scharff[3] have computed a range-energy relation based on elastic nuclear collisions which is also shown in Fig. 3. Our experimental ranges for Ar, Kr, and Xe ions, multiplied by the factor R/R_p, are plotted as vertical lines in Fig. 3; the length of the line indicates the limits of the probable error on each measurement. The N and Ne measurements do not satisfy the requirement $M_1\gg M_0$ and do not appear on the graph. The experimental values are consistently about 20% below the theoretical prediction. Lindhard and Scharff state that electronic contributions to the stopping, which is not included in obtaining the theoretical value of $\mathfrak{R}$, may reduce the range by as much as 20%.

We have computed $(dE/dX)_n$ due to nuclear collisions by differentiating the Lindhard and Scharff $\mathfrak{R}$ values shown in the figure, and added to them the Lindhard and Scharff estimate for the electronic stopping,

$$-(dE/dX)_e=\frac{8\pi NZ_1{}^{7/6}Z_0\hbar^3v}{m_0e^2(Z_1^{\frac{2}{3}}+Z_0^{\frac{2}{3}})^{\frac{3}{2}}}, \tag{10}$$

to obtain a total dE/dX which was integrated to give a range-energy curve. In Fig. 4 we show the resultant range for Xe ions in Be, and our experimental points with the projection correction given above. The improved agreement achieved by including the electronic stopping indicates that electronic stopping, although small, is not negligible.

Insofar as the electronic stopping is small, the range of any ion in any target should fall along the same $\mathfrak{R}$–$\mathcal{E}$ curve. This enables us to compare our results with the measurements by Valyocsik[10] of the range of 96.8-kev Ra^{224} ions in H_2, D_2, He, N_2, Ne, and Ar; and the range of 725-kev Th^{226} ions in D_2, He, N_2, and Ar; and the measurements by Baulch and Duncan[11] of the range of 116-kev Tl^{208} ions in H_2 and Ar. These gas measurements have been plotted as circles in Fig. 3 and show good agreement with the measurements in solids. Davies[12] measurement of the range of 50-kev Cs^{137} ions in Al, plotted as a square in Fig. 3, is higher than our measurements at equivalent $\mathcal{E}$ values.

The Lindhard-Scharff expression for $(dE/dX)_e$ gives a value for 400-kev Ne ions in Be 10 times greater than the nuclear contribution to the stopping, which should be represented at these velocities by Bohr's expression[1]

$$-(dE/dX)_n=\frac{4\pi NZ_1{}^2Z_0{}^2e^4}{M_0v^2}\ln\frac{aM_0M_1v^2}{(M_0+M_1)Z_0Z_1e^2}.$$

Since the stopping is predominantly electronic, we can differentiate our range measurements to obtain dE/dX without a projection correction factor. In the energy range 100–500 kev, our experimental values of dE/dX for Ne ions in Be agree within the experimental uncertainty of $\pm10\%$ with the value of $(dE/dX)_e+(dE/dX)_n$

[10] E. W. Valyocsik, University of California Radiation Laboratory Report, UCRL-8855, 1959 (unpublished).
[11] D. L. Baulch and J. F. Duncan, Australian J. Chem. **10**, 112 (1957).
[12] J. A. Davies, J. D. McIntyre, R. L. Cushing, and M. Lounsbury, Can. J. Chem. **38**, 1535 (1960).

from the expressions above. For N ions in Be in the same energy range, the experimental values are 10–15% below the theoretical values.

ACKNOWLEDGMENTS

We wish to thank Professor J. Lindhard for sending us his range-energy relation prior to publication, Dr. J. C. Overley for the boron targets used in this experiment, and Dr. R. K. Bardin for helpful discussions of proton scattering analysis.

APPENDIX A

Thick-Target Yield Formulas

Let dS represent a thin target lamina parallel to the surface of a thick target as in Fig. 1. This lamina presents a thickness $dS/\cos\theta_1$ to the incident beam. The relation between $dS/\cos\theta_1$ and dE_{20}, the spread in energy accepted by the magnetic spectrometer, was derived by Wenzel[13] for targets of uniform composition:

$$\frac{dS}{\cos\theta_1}=dE_{20}\frac{1}{N}\frac{\epsilon(E_{2S})}{\epsilon(E_{20})}\left[\alpha\epsilon(E_{1S})+\frac{\cos\theta_1}{\cos\theta_2}\epsilon(E_{2S})\right]^{-1}, \quad \text{(A1)}$$

where $\epsilon(E)$ is the total proton stopping cross section per scattering nucleus, and N is the number/cm^3 of scattering nuclei. Since the scattering yield observed in the spectrometer is proportional to $dS/\cos\theta_1$,[14] it follows that the scattering yield from the thin lamina is

$$\mathfrak{N}=\frac{d\sigma}{d\Omega}\Omega_L\frac{2E_{20}}{R_C}Q\frac{\epsilon(E_{2S})}{\epsilon(E_{20})}\left[\alpha\epsilon(E_{1S})+\frac{\cos\theta_1}{\cos\theta_2}\epsilon(E_{2S})\right]^{-1}, \quad \text{(A2)}$$

where $\mathfrak{N}$ is the number of scattered protons detected in the spectrometer for Q protons incident on the target, $d\sigma/d\Omega$ is the cross section for scattering protons through angle θ_L at energy E_{1S}, Ω_L is the solid angle subtended by the entrance aperture of the spectrometer, and R_C is the momentum resolution of the spectrometer.

In the present experiment, the target has been diluted by embedded atoms. If the ratio $\epsilon_I(E)/\epsilon_T(E)$, of the proton stopping cross sections per atom of embedded material and target material, is independent of proton energy, Eq. (A1) can be modified to apply to targets of nonuniform composition:

$$\frac{dS}{\cos\theta_1}=dE_{20}\frac{\epsilon_T(E_{2S})}{\epsilon_T(E_{20})}\left\{\alpha[N_T\epsilon_T(E_{1S})+N_I\epsilon_I(E_{1S})]+\frac{\cos\theta_1}{\cos\theta_2}[N_T\epsilon_T(E_{2S})+N_I\epsilon_I(E_{2S})]\right\}^{-1}, \quad \text{(A3)}$$

where N_T and N_I are the number/cm^3 of target atoms and impurity atoms at a distance S beneath the surface. The thick-target yield formula (A2) can now be written in a form which applies to targets of continuously varying composition:

$$\mathfrak{N}=\frac{d\sigma}{d\Omega}\Omega_L\frac{2E_{20}}{R_C}Q\frac{\epsilon_T(E_{2S})}{\epsilon_T(E_{20})}N\left\{\alpha[N_T\epsilon_T(E_{1S})+N_I\epsilon_I(E_{1S})]+\frac{\cos\theta_1}{\cos\theta_2}[N_T\epsilon_T(E_{2S})+N_I\epsilon_I(E_{2S})]\right\}^{-1}. \quad \text{(A4)}$$

N is either N_I, when the protons observed are scattered from the embedded atoms, or N_T, when scattering from the target atoms is observed.

[13] W. A. Wenzel, Ph.D. thesis, California Institute of Technology, 1952 (unpublished).

[14] C. W. Snyder, S. Rubin, W. A. Fowler, and C. C. Lauritsen, Rev. Sci. Instr. **21**, 852 (1950).